

# Tuning nanoscale heterogeneity by non-affine thermal strain to modulate defect activation and maximize magnetocaloric effect of metallic glass

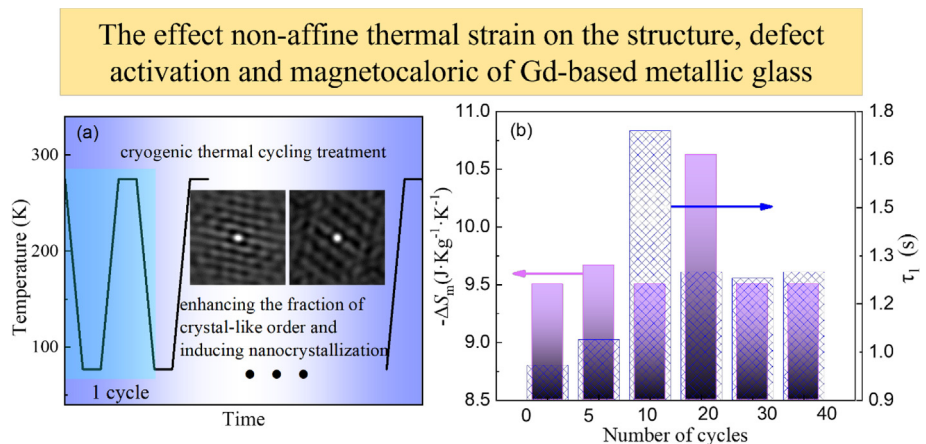
Qiang Luo<sup>\*</sup>, Jingxian Cui, Zhengguo Zhang, Minhao Han, Baolong Shen<sup>\*</sup>

School of Materials Science and Engineering, Jiangsu Key Laboratory for Advanced Metallic Materials, Southeast University, Nanjing 211189, China

## HIGHLIGHTS

- Rejuvenation, increased structure order, and nanocrystallization induced by proper cryogenic thermal cycling are observed.
- Two kinds of flow defects with different relaxation times are detected by using the Maxwell-Voigt model.
- An apparent enhancement of the maximum magnetic entropy change from 9.5 to 10.7 J Kg<sup>-1</sup>K<sup>-1</sup> under 5 T is obtained.
- A power law between the peak temperature and maximum magnetic entropy change is revealed above 85 K.

## GRAPHICAL ABSTRACT



## ARTICLE INFO

### Article history:

Received 2 September 2022

Revised 7 December 2022

Accepted 12 December 2022

Available online 13 December 2022

### Keywords:

Structural heterogeneity

Magnetocaloric effect

Metallic glasses

Relaxation spectrum

## ABSTRACT

The effects of non-affine thermal strain on the structure, defect activation and magnetocaloric effect (MCE) have been investigated in Gd<sub>55</sub>Co<sub>20</sub>Al<sub>24.5</sub>Si<sub>0.5</sub> metallic glass (MG). Maxwell-Voigt models are utilized to analyze the impact of cryogenic thermal cycling (CTC) on the evolution of heterogeneous structure in term of the activated defects during creep deformation. Two kinds of flow defects with different relaxation times are observed from the relaxation spectrum, which show different responses to CTC. A power law between the maximum magnetic entropy change and its peak temperature is uncovered for Gd-based MGs above 85 K, which breaks down below 85 K for the low Gd content MGs including the high-entropy MGs. Through adjusting the CTC number, the maximum magnetic entropy of the present MG is improved to 10.7 J Kg<sup>-1</sup>K<sup>-1</sup> under 5 T, which is the largest among the Gd-based MGs with Curie temperature above 85 K. The enhancement of MCE is related to the increased fraction of solid-like zones in the amorphous matrix and nanocrystallization rendered by CTC treatment. This work sheds new insights into the correlation of MCE and nanoscale creep deformation with structural heterogeneity of MGs.

© 2022 Published by Elsevier Ltd. This is an open access article under the CC BY-NC-ND license (<http://creativecommons.org/licenses/by-nc-nd/4.0/>).

<sup>\*</sup> Corresponding authors.

E-mail addresses: [q.luo@seu.edu.cn](mailto:q.luo@seu.edu.cn), [blshen@seu.edu.cn](mailto:blshen@seu.edu.cn) (B. Shen).

## 1. Introduction

It is well known that heterogeneity like a variety in the short-to-medium range orderings and the coexistence of solid-like and liquid-like regions is the inherent structural feature of MGs [1–2]. And local heterogeneities have also been observed experimentally in the relaxation behavior [3], modulus/hardness [4], viscoelasticity [5], and density [6,7]. Although it is difficult for accurate analyses, tailoring and characterizing the heterogeneity have been widely used to enhance and understand the physical and mechanical properties [2,8–10]. Recently, cryogenic thermal cycling (CTC) treatment was proved to be a simple and effective method for rejuvenating MGs and enhancing their plasticity, which was correlated with the more heterogeneity introduced [11]. Although intensive work has been devoted to exploring the effect of CTC on MGs [12,13], the evolution of heterogeneities upon CTC is still elusive, and a distinct relationship between the heterogeneities (such as the flow defects, solid/liquid-like zones) and macroscopic mechanical/physical properties of MGs remains unknown.

Besides, the influence of CTC on the magnetic performances of MGs is much less investigated than that on the mechanical behavior. It was reported that CTC improved the bending ductility but had little effect on the soft magnetic property in the annealed Fe-Co-Si-B-Cu MG [14]. But in the Fe-Si-B-Cu MG, increased saturation flux density and thermal stability, more compacted structure, and decreased coercivity were observed after CTC [15]. In the Fe-Si-B MG, the magnetic properties showed an apparent fluctuation with increasing number of CTC, which implied the CTC-induced stochastically rejuvenation or aging [16]. These investigations indicate

that the sensitivity of magnetic properties to CTC treatment depends on MG's composition. However, the effect of CTC on the MCE performance of MG has not been reported yet, and previous investigations focus on effects of composition design and various post treatments (such as normal annealing, hydrogenation, current annealing, etc.) for partial crystallization [17–20]. Recently, it was found that annealing below the glass transition temperature can increase the magnetocaloric performance of some MGs due to the increased fraction of crystal-like medium-range order without crystallization [21]. And different MCE properties were observed in the ribbon, bulk rod, and microwire samples with the same composition but distinct medium ranges orders, and several advantages of properties are reported in the microwire samples with unique composite structure [22–25]. These works indicate the significant role of nanoscale/ micrometer-scale structural heterogeneity on MCE performance of MGs and related composites.

Here, we tune the heterogeneity, defect activation during creep deformation, and MCE of a magnetocaloric MG by cryogenic thermal cycling (CTC) treatment. Rejuvenation, increased structure order, and nanocrystallization induced by proper CTC are observed. In virtue of nanoindentation techniques, evolution of structure heterogeneity during creep deformation was detected and the different contributions of solid-like and liquid-like regions to MCE can be revealed. Distinct responses of the two kinds of flow defects to CTC are observed. The underlying mechanisms of the nanoscale creep behaviors were discussed. Significantly, an obvious change ( $\sim 7$  K) of the Curie temperature and an apparent enhancement of the maximum magnetic entropy change from 9.5 to 10.7  $\text{JK}^{-1}$  under 5 T are obtained. It is revealed that the variation of

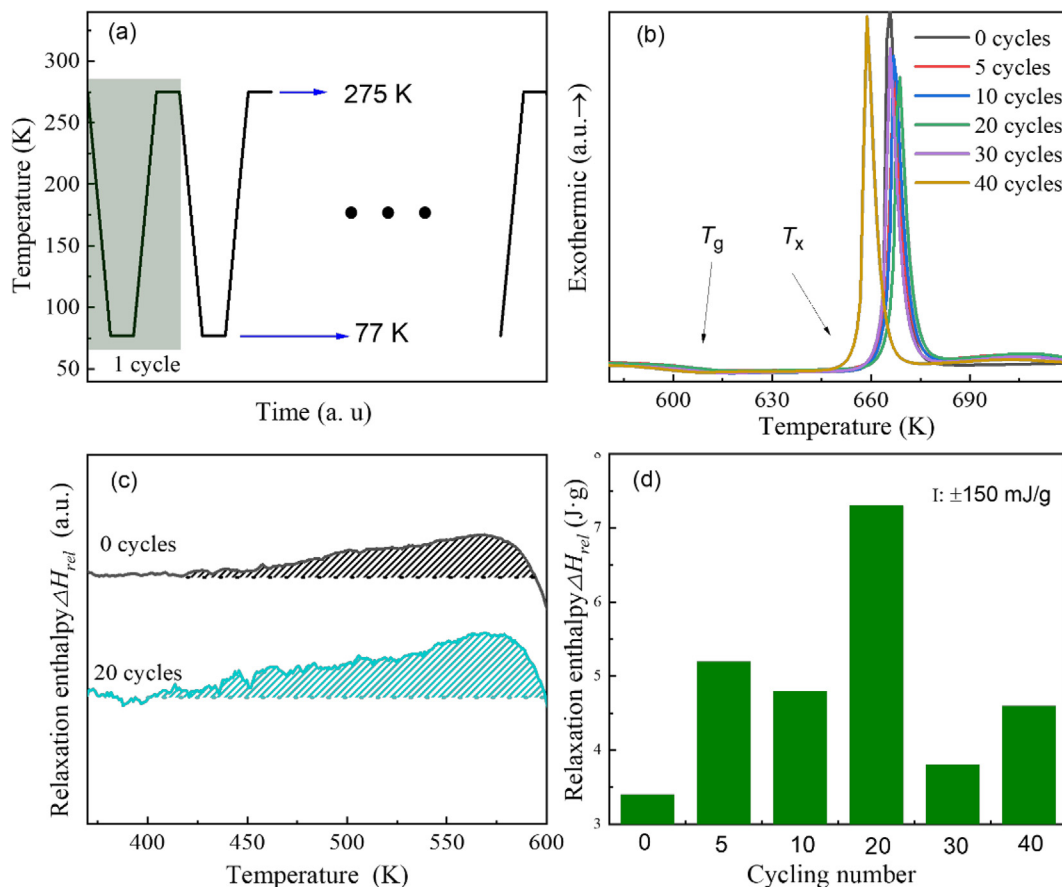


**Fig. 1.** (a) Schematic map of the thermal cycling treatment between 275 and 77 K. (b) DSC curves of the as-cast and CTC treated samples at a heating rate of 20 K/min showing the glass transition and crystallization events. (c) Near- $T_g$  DCS curves of the as-cast and 20 cycles-treated samples showing how the relaxation enthalpy is determined. (d) Relaxation enthalpy of the as-cast and CTC treated samples with error range of  $\pm 150$  mJ/g.

the solid-like zones plays a more important impact than the liquid-like zones on the change of MCE. Besides, a power law between the peak temperature and maximum magnetic entropy change in Gd-based MGs and Gd-contained high entropy MGs is revealed above 85 K but breaks down below 85 K by the high configuration entropy effect. The summary plot may indicate a limiting value (close to  $10.7 \text{ Jkg}^{-1}\text{K}^{-1}$  under 5 T obtained here) of the magnetic entropy change in Gd-based MGs with Cure temperature above 85 K.

## 2. Experimental section

$\text{Gd}_{55}\text{Co}_{20}\text{Al}_{24.5}\text{Si}_{0.5}$  MG rod with 2 mm in diameter was prepared by copper mold suction casting method using a mixture of raw materials with purities above 99.9 wt%. Differential scanning calorimetry (DSC, NETZSCH 404 F3) experiments were performed at a heating rate of 20 K/min to determine the glass transition temperature ( $T_g$ ), crystallization temperature ( $T_x$ ), and relaxation enthalpy ( $\Delta H_{rel}$ ). The rods were cut into slices with thickness of 1 mm for CTC treatments. Then the slices were subjected to different temperature cycles (5,10,20,30,40) between 77 and 275 K. The dwelling time at 77 K (or 275 K) is one minute. The hardness  $H$  and indentation modulus  $E_r$  were measured by using NanoTest Vantage (Micro Materials Ltd) with a standard Berkovich diamond indenter, whose load and displacement resolutions were 3 nN and 0.001 nm, respectively. A loading rate of 5 mN/s was used, and the maximum load was 50 mN. For each sample,  $8 \times 8$  points were measured for distribution analysis of the hardness. Creep measurements were conducted as following: the sample was loaded at a loading rate of 10 mN/s to the maximum load of 50 mN followed by a holding period of 120 s, and then unloaded at 10 mN/s. Five independent measurements were carried out for each sample. Magnetic properties were measured by using a Magnetic Properties Measurement System (MPMS, Quantum Design). The temperature dependence of magnetization was measured on heating from 20 to 150 K under 500 Oe after cooling the sample to 20 K under the same field (ie. FC mode). The isothermal magnetization curves were recorded from 0 to 5 T with a slow sweeping rate of field to ensure the data are recorded in an isothermal process at different temperatures. The structure feature was characterized by Transmission electron microscope (TEM, Tecnai G20, FEI). And the TEM samples were prepared by ion milling method (Gatan Inc., PIPS-M691) under liquid nitrogen condition.

## 3. Results and discussion

The CTC experiment for different cycles is illustrated in Fig. 1(a). To avoid the effects of  $\beta$  and  $\alpha$  relaxation (relating to a locally initiated reversible process and a large scale irreversible structural rearrangement, respectively) [2], the high temperature end of the CTC treatment is chosen to be 273 K. Fig. 1(b) presents the DSC curves of the as-cast and treated samples, showing clear glass transition and crystallization events. The glass transition temperature ( $T_g$ ) and the onset temperature of crystallization temperature ( $T_x$ ) of the as-cast sample are determined to be 592 and 657 K, respectively. The crystallization peak shows larger change than the glass transition event after CTC treatment. With increasing cycling number, the  $T_x$  increases from 657 K to a maximum of 661 K for the 20 cycles-treated sample and decreases afterwards to a minimum of 649 K for the 40 cycles-treated sample, indicating a remarkable change of the local structure. Furthermore, the relaxation enthalpy ( $\Delta H_{rel}$ ) was calculated from the DSC curves, as illustrated in the shaded areas in Fig. 1(c) for the as-cast and 20 cycles-treated samples. The  $\Delta H_{rel}$  have been widely used to investigate the relaxation dynamics and characterize the effects of thermal/mechanical post

treatments on MGs [9,11]. As seen from Fig. 1(d), the  $\Delta H_{rel}$  increases after CTC treatment for 5 cycles, obtaining a peak at 20 cycles, and decreases afterward. The increase of  $\Delta H_{rel}$  after CTC indicates the rejuvenation of the amorphous structure into a higher energy state with more heterogeneity, which relates to the stress generated from spatially nonuniform distribution of temperature between surfaces and interiors [11].

It has been reported that CTC can cause rejuvenation or relaxation of MGs, and improve or degrade their mechanical properties, depending on the CTC condition and alloy's composition [11,26]. This complexity is related to the diverse structural/mechanical heterogeneities of MGs at short-to-medium range orders [11,26]. To investigate the change of heterogeneity of the present magneto-caloric Gd-based MG after CTC, nanoindentation experiments were carried out. The load–displacement curves of the as-cast and some CTC treated samples were collected from 64 different points ( $8 \times 8$  array). Typical load–displacement curves are shown in Fig. 2(a). Some “pop-in” events are observed in the loading curves, which originate from the initiation/expansion of the shear bands underneath the indenter. Since the initial yield pressure cannot be well identified for some curves, we analysis the distribution of hardness. Clear spatial fluctuation of the hardness is observed

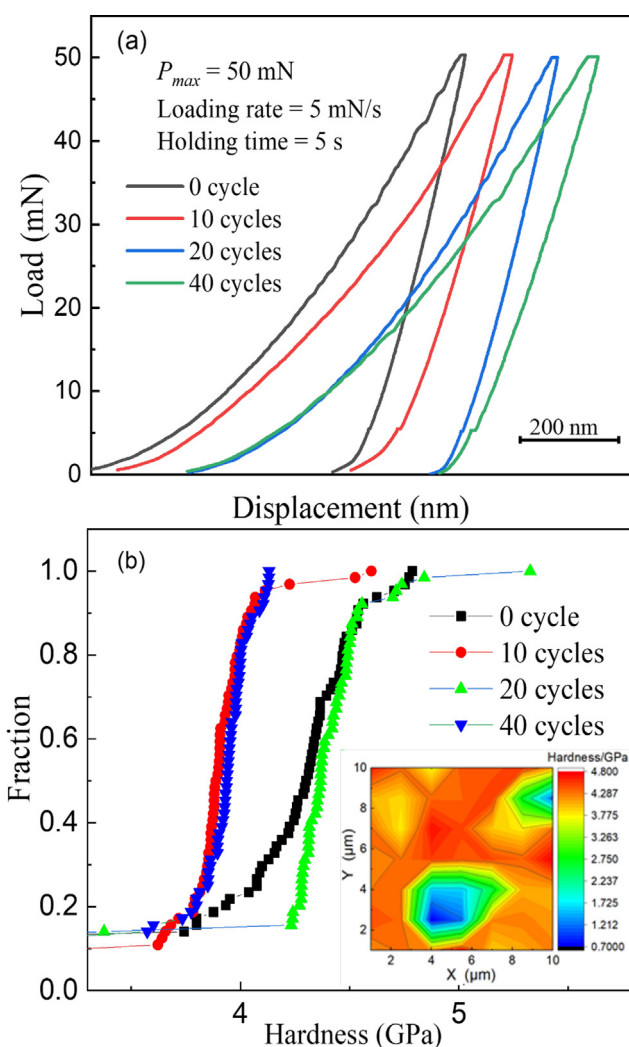


**Fig. 2.** (a) Typical load–displacement ( $P$ - $h$ ) curves of the as-cast and some CTC treated samples. (b) Cumulative distributions of the hardness for the as-cast and some CTC treated samples, the inset shows the contour-line map of the hardness for the as-cast sample.

from its 2-D contour map for the as-cast sample in the inset of Fig. 2(b). The change of mechanical heterogeneity in these samples can further be evaluated by the cumulative distribution curves of the hardness in Fig. 2(b). The average hardness decreases after CTC treatment for 10 and 40 cycles but increases for 20 cycles. The above results imply that CTC for 20 cycles not only induces obviously structural rejuvenation but also increases the fraction of dense-packed local regions.

The evolution of structural heterogeneity during creep deformation is further explored by analyzing the relaxation time spectrum obtained from the nanoindentation method. The Maxwell-Voigt model is used to describe the creep deformation under indentation process [27–29], and a schematic diagram of the model including one Maxwell unit and two Kelvin units is illustrated in Fig. 3(a). A typical creep curve and its fitting by this model is shown in Fig. 3(b) for one CTC treated sample. The creep displacement curve contains a rapidly increasing primary creep stage, where the two Kelvin units dominate, and the steady-state stage in which Maxwell dashpot acts as the dominant role. The fitting equation is:

$$H(t) = h_1(1 - e^{-t/\tau_1}) + h_2(1 - e^{-t/\tau_2}) + t/\mu_0 \quad (1)$$

where  $h_i$  the indentation depth and  $\tau_i$  the characteristic relaxation time of the  $i$ -th anelastic Kelvin unit,  $t$  is the holding time, and  $\mu_0$  the viscoelastic constant of the Maxwell dashpot. It is generally accepted that the two characteristic relaxation time  $\tau_1$  and  $\tau_2$  correlate with the different kinds of flow defects in the liquid-like and solid-like regions [28]. From Fig. 3(b), the above model can describe the nanoscale creep behavior of present Gd-based MG very well.

Based on the Maxwell-Voigt model, the relaxation time spectrum or creep retardation spectra can be obtained from the following approximated equation to describe the two anelastic creep processes of the samples [28,29]:

$$L(\tau) = \left[ \sum_{i=1}^n \left( 1 + \frac{t}{\tau_i} \right) \frac{h_i}{\tau_i} e^{-\frac{t}{\tau_i}} \right] \frac{A_0}{P_0 h_{in}} t|_{t=2\tau} \quad (2)$$

where  $L$  is the spectrum intensity,  $A_0/P_0$  the inverse of hardness, and  $h_{in}$  the maximum indentation depth. The  $t$ ,  $h_i$ , and  $\tau_i$  are the same parameters used in Eq. (1), and  $n = 2$ . As indicated in Fig. 3, each relaxation spectrum of all the samples shows two separate peaks, which correspond to the two relaxation processes with characteristic relaxation time  $\tau_1$  and  $\tau_2$ . Both the intensity and relaxation time of the two peaks change notably by the CTC treatment as shown in Fig. 3(c). The peak intensity of  $\tau_1$  first increases with increasing cycle number to a maximum around 20 cycles, and then decreases gradually (Fig. 4(a)). Differently, the peak intensity of  $\tau_2$  increases with increasing cycles to a maximum around 30 cycles and shows a slight decrease for the 40 cycles-treated sample. These results imply that more defects in both the liquid-like and solid-like regions are activated with proper CTC treatment. Moreover, the  $\tau_1$  value shows a maximum around 10 cycles, presenting an increase-then-decrease trend of the size of the activated defects in the solid-like region with increasing cycles (Fig. 4(b)). In contrast,  $\tau_2$  increases gradually with increasing cycles, indicating the continuously increasing size of activated defects in the liquid-like region. The distinct responses of the two kinds of flow defects to the CTC treatment are attributed to their different coefficients of thermal

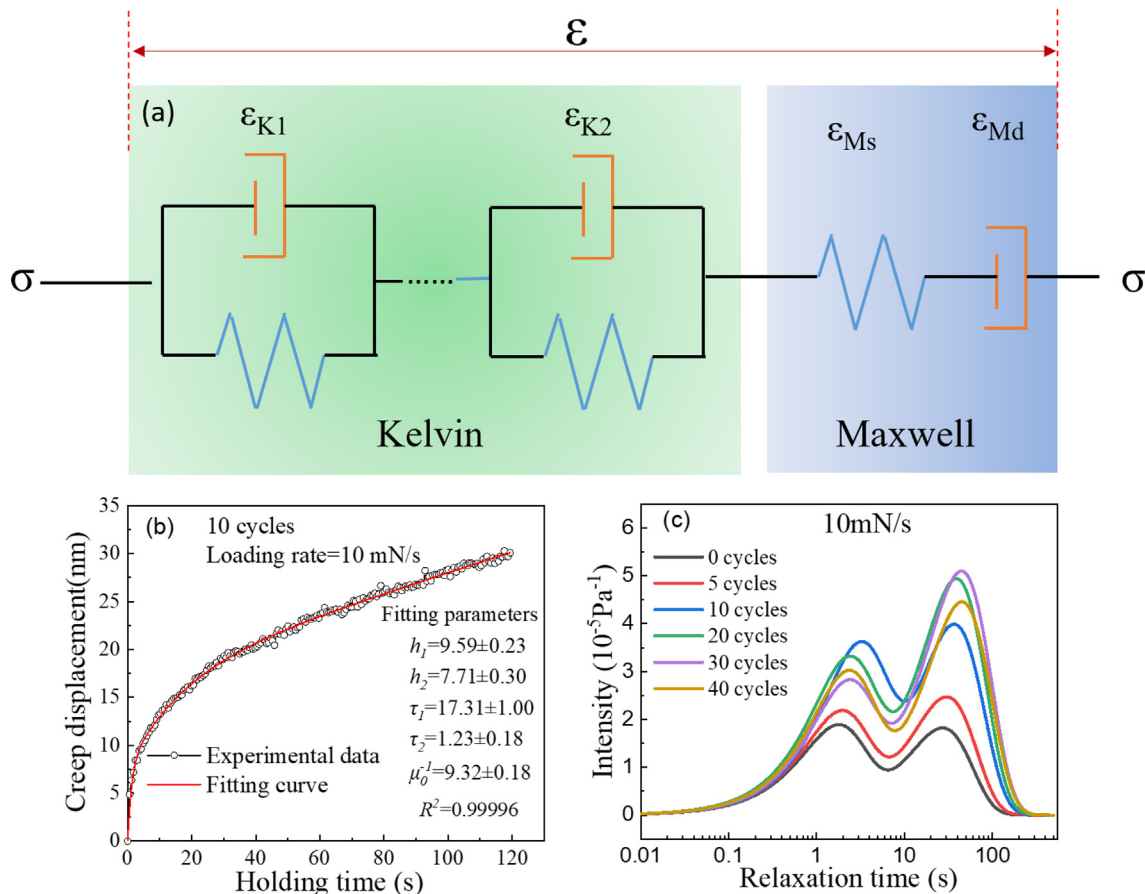


Fig. 3. (a) The Maxwell-voigt model used for analyzing the creep curves. (b) Typical creep curve of the sample treated for 10 cycles and the corresponding fitting curve. (c) Relaxation spectrum of the as-cast and CTC treated samples.

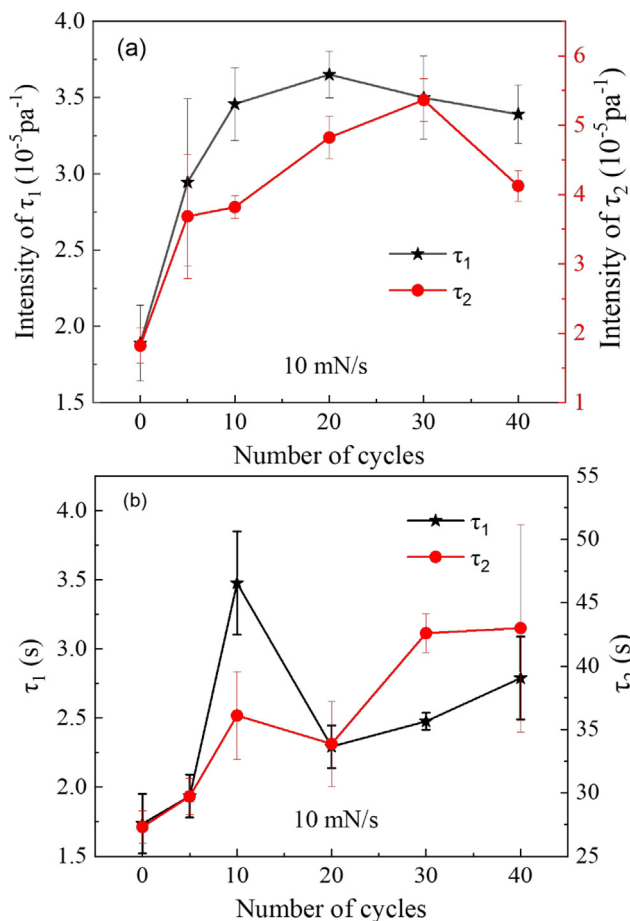


Fig. 4. Variation of the position and intensity of the first and second peaks in the relaxation spectrum with the cycling number.

expansion and local environments in solid-like and liquid-like regions.

Then we explore the effect of structural heterogeneity change on the MCE performance. Fig. 5 presents the temperature dependence of the field cooled (FC mode) magnetization, which was measured on heating under 500 Oe after initially cooling to 20 K under 500 Oe. All the samples show a paramagnetic-to-ferromagnetic transition, which is typical for Gd-based MGs [11,18]. From the minimum of  $dM/dT$ , the Curie temperature ( $T_c$ ) can be determined and its variation with CTC is shown in the inset of Fig. 5(a). After 5 cycles,  $T_c$  decreases from 104 to 97 K, keeping almost unchanged up to 30 cycles, and then increases to 104 K at 40 cycles, indicating the significant impact of the structural heterogeneity on the magnetic interactions (among Gd atoms). In addition, the relatively sharp change of magnetization around  $T_c$  and large effective magnetic moments of Gd atom imply a large MCE in all these samples.

Typical isothermal magnetization curves with increasing field from 0 to 5 T in a temperature range of 90–108 K with a step of 3 K for the as-cast sample are presented in Fig. 5(b). The magnetization increases rapidly in the low field range and then approaches saturation gradually, as is observed in other Gd-based MGs [11,18]. The Arrott plots obtained from the isothermal magnetization curves are shown in the inset of Fig. 5(b). The slopes of all the curves are positive and no inflection point is observed, indicating a second-order phase transition nature based on the Banerjee criterion [30]. All the other CTC treated samples show similar features. Then the magnetic entropy change ( $-\Delta S_m$ ) of the samples

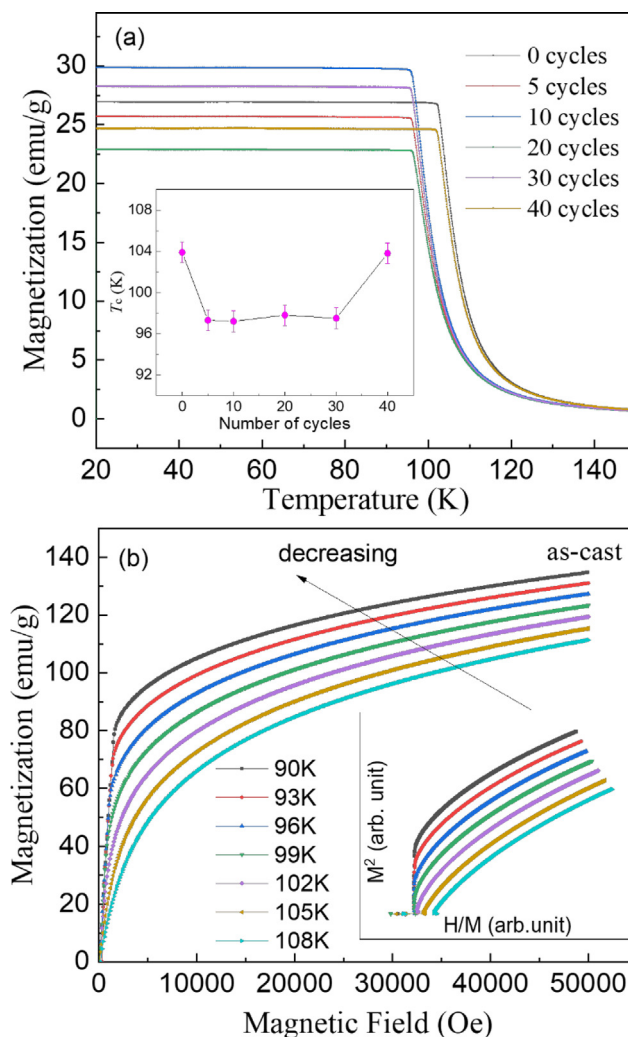


Fig. 5. (a) Temperature dependence of the magnetization, and the inset show the cycling number dependence of the Curie temperature. (b) Isothermal magnetization of the as-cast sample, and the inset shows the corresponding Arrott plot.

is derived from Maxwell relations. It can be seen in Fig. 6(a) that CTC tunes the MCE performance obviously both in the maximum magnetic entropy change and peak temperature. The peaks of the magnetic entropy change curves locate around the  $T_c$  determined from Fig. 5(a). Significantly, the maximum magnetic entropy change increases from  $9.5 \text{ J Kg}^{-1} \text{ K}^{-1}$  for the as-cast sample to  $10.7 \text{ J Kg}^{-1} \text{ K}^{-1}$  for the 20 cycles-treated sample (Fig. 6(b)). Treatment with more CTC cycles leads to a reduction of the magnetic entropy change to the as-cast level. The sensitivity of MCE performance to the CTC is reminiscent of the changes of plasticity and relaxation enthalpy upon CTC, which are sensitive to the temperature interval and number of cycles [26].

Fig. 7 compare the maximum magnetic entropy changes under a field change of 5 T of present sample with other typical Gd-based MGs (mainly those without a second rare earth element for simplicity) and the Gd-contained high entropy MGs [28–51]. The present 20 cycles-treated sample possesses the largest maximum magnetic entropy change among the listed MGs in the temperature range above 85 K. The increase of  $1.2 \text{ J Kg}^{-1} \text{ K}^{-1}$  is of significance since the maximum magnetic entropy change under a field change of 5 T in some Fe- and Pd-based MGs is less than  $1 \text{ J Kg}^{-1} \text{ K}^{-1}$  [52,53]. Besides, the summary plot suggests that there exists a limiting value of the maximum magnetic entropy change in Gd-based

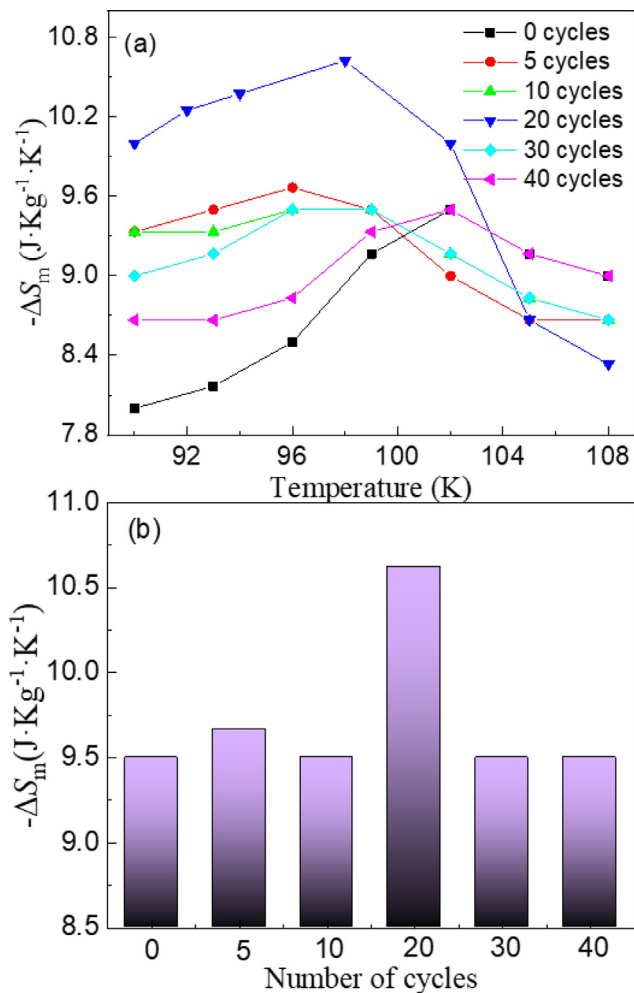


Fig. 6. (a) Temperature dependence of the magnetic entropy change. (b) Variation of the maximum magnetic entropy change with cycling number.

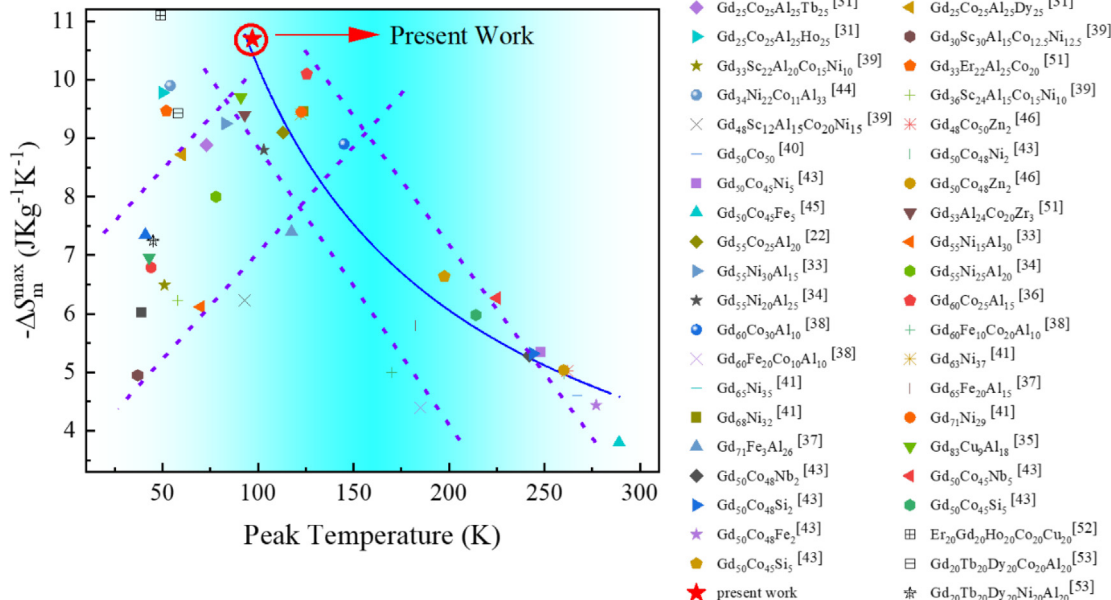


Fig. 7. Relation between the peak temperature and the maximum magnetic entropy change of typical Gd-based MGs including the Gd contained high-entropy MGs. The dashed lines are only used to guide the eyes and the blue full line is the fitting curve by a power-law relation. (For interpretation of the references to colour in this figure legend, the reader is referred to the web version of this article.)

MGs with Curie temperature above 85 K (close to  $10.7 \text{ JKg}^{-1}\text{K}^{-1}$  under 5 T obtained here). Enhancing the content of Fe/Co can increase the curie temperature but decrease the magnetic entropy change considerably. By introducing other kinds of rare earth elements or using the high entropy design strategy may increase  $-\Delta S_m$  at the cost of reducing the working temperature considerably. This implies that composite design strategy should be used in the future to further enhance the MCE performance around the peak temperature region of Fig. 7.

Next, we discuss the relation between  $-\Delta S_m$  and  $T_p$  (the peak temperature of  $-\Delta S_m$ ) presented in Fig. 7. Based on the molecular mean field model, a power-law relation between  $-\Delta S_m$  and  $T_c$  was suggested ( $-\Delta S_m \propto T_c^{-2/3}$ ) [54], which was observed in many crystalline magnetic systems in a narrow composition range [17]. Different systems may present different slopes of the  $-\Delta S_m-T_c^{-2/3}$  curve due to their different microscopic parameters such as Curie temperature, magnetic moment, and magnetic exchange interactions [17]. In some Gd-Cd MGs, the linear dependence of  $\Delta S_m$  on  $T_c^{-2/3}$  was obtained in a narrow  $T_c$  range [43]. Interestingly, Fig. 7 indicates that above 85 K, a power law relation with an index of  $-0.74$  (better than using an index of  $-1$  or  $-2/3$ ) works roughly for a broad range of compositions with peak temperatures covering from 85 to 298 K (see the full blue line). Considering these MGs are different in many respects such as compositions, cooling rates, sample dimension, and magnetic interactions, this correlation is remarkable and of significance. Note that the two high Fe content alloys  $\text{Gd}_{60}\text{Fe}_{10}\text{Co}_{20}\text{Al}_{10}$  and  $\text{Gd}_{60}\text{Fe}_{20}\text{Co}_{10}\text{Al}_{10}$  show a relatively larger deviation from the power law because of the existence of some crystalline phase in the amorphous matrix [38]. Moreover, such a power law breaks down below 85 K, and the overall increase of  $-\Delta S_m$  with increasing  $T_p$  cannot be illustrated by the mean field mode. However, a few compositions beyond the trend are also observed, indicating the delicate role of local configurations and magnetic interactions on the MCE. Recently, it was found that high configuration entropy in high entropy rare earth-based MGs is not beneficial for enhancement of MCE, and their magnetic behavior mainly depends on the complex intrinsic magnetic interactions [55]. It was suggested that the strong chemical disorder due to high

configuration entropy may retard magnetic phase transition in some high entropy alloys [56]. The low-temperature part of Fig. 7 indicates that high configuration entropy presents a subtle role on the local structural and magnetic configurations. The decrease of  $-\Delta S_m$  with decreasing peak temperature may arise from the decreased ferromagnetic exchange interaction due to reduced Gd concentration and increased random magnetic anisotropy from other rare earth elements [32]. At present, the detailed mechanisms of the breakdown of the power-law below 85 K is not clear, needing further theoretical and experimental investigations.

Then, we discuss the possible origin of the enhanced maximum of  $-\Delta S_m$  after CTC treatment for 20 cycles. CTC contains expansion process upon heating and contraction processes upon cooling. For MGs with considerable diversity in the short-to-medium range ordered structures, heterogeneous contraction or thermal expansion occurs during CTC [26], which produces local stresses and changes the liquid-like and solid-like zones differently through local atomic arrangements. This is the reason why different responses of the first and second peaks in the relaxation spectrum to CTC are observed. Note that the first characteristic relaxation time, instead of the second one, shows the similar cycling number dependence to the peak magnetic entropy change. This implies that local structure change in the solid-like zones plays a more important role than in the liquid-like zone on the variation of magnetic entropy change. It is reasonable to argue that the Gd-Gd pairs in the solid-like zones have shorter instance and thus stronger exchange interactions than the liquid-like zones, playing more sig-

nificant impact on the magnetic performance. Thus, the enhancement of MCE after treatment for 20 cycles may arise from the increased fraction of solid-like defects (such as local structures with crystal-like order, possible nanocrystalline grains, etc.) in the matrix.

HRTEM observation was further conducted to examine the change of atomic structure. As indicated in Fig. 8(a), the HRTEM pattern of the as-cast sample is disordered and maze-like, showing typical amorphous feature, which is according with the selected area electron diffraction (SAED) patterns (the inset). However, nanocrystals with size of 3–5 nm can be observed in the HRTEM of the 20 cycles-treated sample (Fig. 8(b)). Correspondingly, the SAED shows thinner diffraction rings and diffraction spots. To further evaluate the change of local structure order, the HRTEM image is divided into 100 square boxes with a side length of 1.985 nm (typical size of medium range order [57]) and transformed into 2D auto correlation images [58]. Typical sub-images with amorphous-like order with maze-like feature, crystal-like order with obvious symmetric fringe, and nanocrystal are shown in Fig. 8(c), (e), and (g), respectively. The FFT patterns of Fig. 8(c), (e), and (g) are shown in Fig. 8(d), (f), and (h), respectively. Some spots can be detected in Fig. 8(f) and more spots appear in the FFT pattern of the nanocrystal in Fig. 8(h). All the square sub-images from Fig. 8(a, b) are analyzed by the above method. The segmentations of the HRTEM images of the as-cast and 20 cycles-treated samples are present in Fig. 8(i) and (j), respectively, in which the sub-images with crystal-like order are marked by red

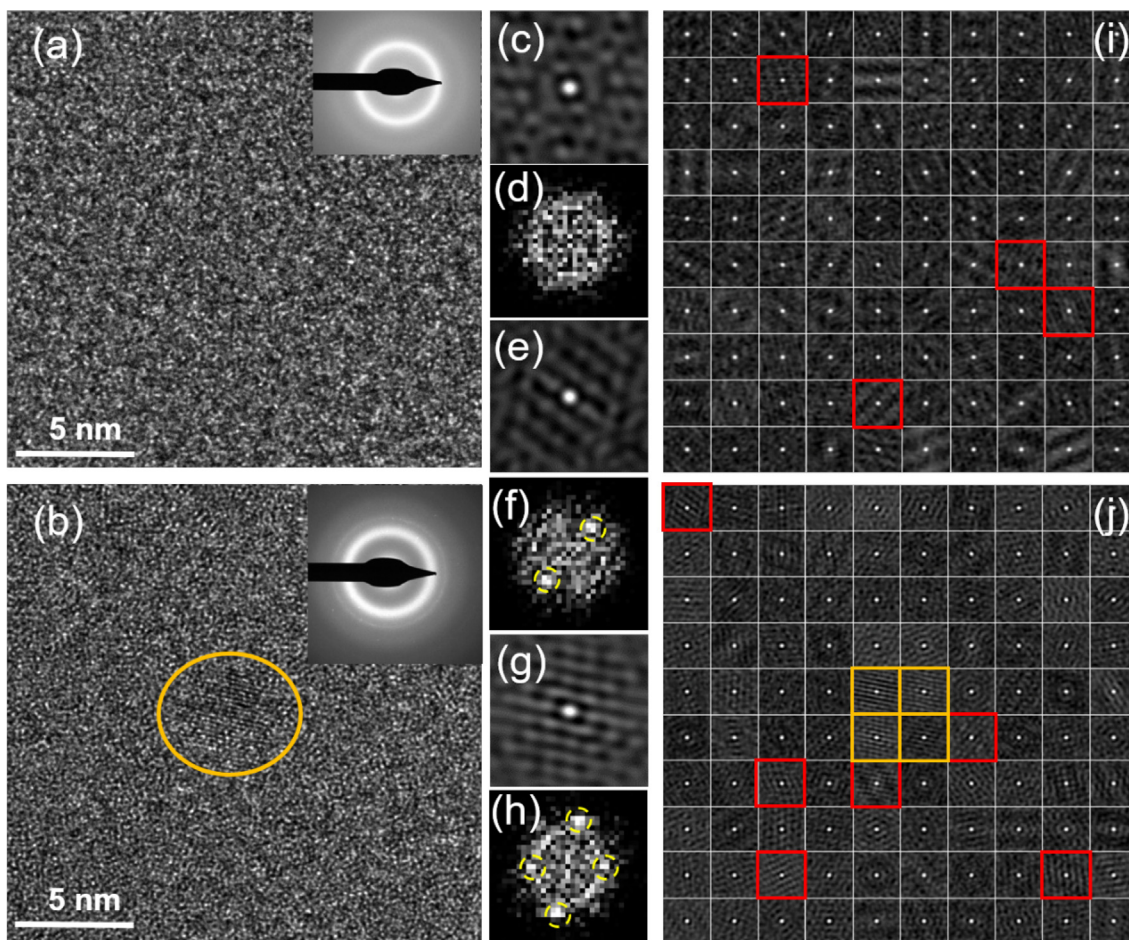


**Fig. 8.** HRTEM images of as-cast sample (a) and sample CTC treated with 20 cycles (b), the insets are the FFT patterns. (c), (e), and (g), are the auto-correlation maps of the typical cells with amorphous, crystal-like-order and nanocrystalline structures, respectively. (d), (f), and (h) are FFT patterns of cells (c), (e), and (g), respectively. Auto-correlation images (i and j) obtained from the HRTEM of the as-cast (a) and 20 cycles-treated samples (b), respectively.

frame, and those for the nanocrystals by yellow frame. Thus, the area fractions of these crystal-like and nanocrystal domains in the as-cast and 20 cycles-treated samples can be determined to be  $\sim 4\%$  and  $10\%$ , respectively. Accordingly, CTC enhances the fraction of crystal-like local order and renders nanocrystal formation, which contributes to the increased intensity of the activated hard defects (the first peak in the relaxation spectrum) and increased hardness (Fig. 2(b)). Certainly, the increased fraction of the other solid-like regions in the amorphous matrix also plays a significant role [21]. In a Gd-Al-Ni bulk MG, it was observed that the peak magnetic entropy change increased after formation of some intermediate phases by annealing above  $T_g$  [59]. In present work, the CTC, instead of annealing, is adopted to enhance the structural order, form nano-crystallized (NC) structures, and enhance the fraction of solid-like regions, which promote synergistically to the increased peak magnetic entropy of the 20 cycles-treated sample.

In conclusion, local stress arising from the heterogeneous thermal contraction/expansion during CTC renders structure rejuvenation, heterogeneous atomic arrangement, and nanocrystallization in  $Gd_{55}Co_{20}Al_{24.5}Si_{0.5}$  MG. The anelastic and viscoplastic deformation during nanoscale creep process can be well described by the Maxwell-Voigt model. Both the size and number of activated flow defects in solid-like and liquid-like regions present distinct variations to CTC. The MCE and the first peak of relaxation spectra (correlated with response of the defects in solid-like region) show a similar varying trend with the cycling number. This may imply the local structure change in the solid-like zones plays a more important impact than the liquid-like zones on the variation of magnetocaloric properties. Significantly, proper CTC improves the peak magnetic entropy of the MG to the top of the  $\Delta S_m-T_p$  curve of Gd-based MGs reported, which is associated with the combined effects of increased local structure ordering, nanocrystallization and enhanced fraction of solid-like region. This study throws new light on the nature of MCE in MGs and provides a fundamental guideline for optimizing MCE by controlling the structural heterogeneity. The complicated changes of the investigated properties after CTC, and the non-monotonic relationship of  $\Delta S_m$  vs  $T_p$  indicate that a complex picture should be established on the interplays among composition, non-affine thermal strain, atomic/magnetic configurations, and MCE performance.

### Data availability

Data will be made available on request.

### Declaration of Competing Interest

The authors declare that they have no known competing financial interests or personal relationships that could have appeared to influence the work reported in this paper.

### Acknowledgement

This work was supported by the National Natural Science Foundation of China (Grant Nos. 51971061 and 52231005) and Natural Science Foundation of Jiangsu Province (BK20221474).

### References

- [1] H.W. Sheng, W.K. Luo, F.M. Alamgir, et al., Atomic packing and short-to-medium range order in metallic glasses, *Nature* 439 (2006) 419–425.
- [2] J.C. Qiao, Q. Wang, J.M. Pelletier, et al., Structural heterogeneities and mechanical behavior of amorphous alloys, *Prog. Mater. Sci.* 104 (2019) 250–329.

- [3] P. Zhang, J.J. Maldonis, Z. Liu, et al., Spatially heterogeneous dynamics in a metallic glass forming liquid imaged by electron correlation microscopy, *Nat. Commun.* 9 (2018) 1129.
- [4] H. Wagner, D. Bedorf, S. Kuchemann, et al., Local elastic properties of a metallic glass, *Nat. Mater.* 10 (2011) 439–442.
- [5] Q. Luo, Z.G. Zhang, D.H. Li, et al., Nanoscale-to-mesoscale heterogeneity and percolating favored clusters govern ultrastability of metallic glasses, *Nano Lett.* 22 (2022) 2867–2873.
- [6] B. Huang, T.P. Ge, G.L. Liu, et al., Density fluctuations with fractal order in metallic glasses detected by synchrotron X-ray nano-computed tomography, *Acta Mater.* 155 (2018) 69–79.
- [7] F. Zhu, A. Hirata, P. Liu, et al., Correlation between local structure order and spatial heterogeneity in a metallic glass, *Phys. Rev. Lett.* 119 (2017) 215501.
- [8] Q. Luo, D.H. Li, M.J. Cai, et al., Excellent magnetic softness-magnetization synergy and suppressed defect activation in soft magnetic amorphous alloys by magnetic field annealing, *J. Mater. Sci. Technol.* 116 (2022) 72–82.
- [9] S.Y. Di, Q.Q. Wang, J. Zhou, et al., Enhancement of plasticity for FeCoBSiNb bulk metallic glass with superhigh strength through cryogenic thermal cycling, *Scr. Mater.* 187 (2020) 13–18.
- [10] Q. Luo, W.H. Wang, Magnetocaloric effect in rare earth-based bulk metallic glasses, *J. Alloy. Compd.* 495 (2010) 209–216.
- [11] S.V. Ketov, Y.H. Sun, S. Nachum, et al., Rejuvenation of metallic glasses by non-affine thermal strain, *Nature* 524 (2015) 200–203.
- [12] Y. Tang, H.B. Biao, X.D. Wang, et al., Mechanical property and structural changes by thermal cycling in phase-separated metallic glasses, *J. Mater. Sci. Technol.* 78 (2021) 144–154.
- [13] P. Ross, S. Kuchemann, P.M. Derlet, et al., Linking macroscopic rejuvenation to nano-elastic fluctuations in a metallic glass, *Acta Mater.* 138 (2017) 111–118.
- [14] H. Zheng, L. Zhu, S.S. Jiang, et al., Recovering the bending ductility of the stress-relieved Fe-based amorphous alloy ribbons by cryogenic thermal cycling, *J. Alloy. Compd.* 790 (2019) 529–535.
- [15] Y. Meng, Y.G. Wang, L. Zhu, et al., Effect of thermal cycling treatment on local structure, thermal stability and magnetic properties of  $Fe_{80}Si_{8.75}B_{10}Cu_{1.25}$  metallic glass, *J. Non Cryst. Solids* 471 (2017) 406–409.
- [16] M.C. Ri, S. Sohrabi, D.W. Ding, et al., Serrated magnetic properties in metallic glass by thermal cycle, *Chin. Phys. B* 6 (2017) 066101.
- [17] V. Franco, J.S. Blázquez, J.J. Ipús, et al., Magnetocaloric effect: From materials research to refrigeration devices, *Prog. Mater. Sci.* 93 (2018) 112–232.
- [18] X.C. Zhong, H.Y. Yu, Z.W. Liu, et al., Influence of crystallization treatment on structure, magnetic properties and magnetocaloric effect of  $Gd_{71}Ni_{29}$  melt-spun ribbons, *Curr. Appl. Phys.* 18 (2018) 1289–1293.
- [19] B. Yin, J.Y. Law, Y. Huang, et al., Enhancing the magnetocaloric response of high-entropy metallic-glass by microstructural control, *Sci. China Mater.* 65 (2022) 1134–1142.
- [20] H. Fu, M. Zou, N.K. Singh, Modification of magnetic and magnetocaloric properties of Dy-Co-Al bulk metallic glass introduced by hydrogen, *Appl. Phys. Lett.* 97 (2010) 262509.
- [21] L.L. Shao, L. Xue, Q. Luo, et al., The role of Co/Al ratio in glass-forming GdCoAl magnetocaloric metallic glasses, *Materialia* 7 (2019) 100419.
- [22] P. Yu, N.Z. Zhang, Y.T. Cui, et al., Achieving an enhanced magneto-caloric effect by melt spinning a  $Gd_{55}Co_{25}Al_{20}$  bulk metallic glass into amorphous ribbons, *J. Alloy. Compd.* 655 (2016) 353–356.
- [23] H.X. Shen, H. Wang, J.S. Liu, et al., Enhanced magnetocaloric properties of melt-extracted GdAlCo metallic glass microwires, *J. Magn. Magn. Mater.* 372 (2014) 23–26.
- [24] R. Varga, T. Ryba, Z. Vargova, et al., Magnetocaloric effects in magnetic microwires for magnetic refrigeration applications, in: *Magnetic Nano- and Microwires: Design, Synthesis, Properties and Applications*, Woodhead Publishing, Sawston, Cambridge, 2015, pp. 569–587.
- [25] J. Alam, C. Bran, H. Chiriac, et al., Cylindrical micro and nanowires: fabrication, properties and applications, *J. Magn. Magn. Mater.* 513 (2020) 167074.
- [26] S.V. Ketov, A.S. Trifonov, Y.P. Ivanov, et al., On cryothermal cycling as a method for inducing structural changes in metallic glasses, *NPG Asia Mater.* 10 (2018) 137–145.
- [27] B.G. Yoo, I.C. Choi, Y.J. Kim, et al., Room-temperature anelasticity and viscoplasticity of Cu-Zr bulk metallic glasses evaluated using nanoindentation, *Mater. Sci. Eng.-A* 577 (2013) 101–104.
- [28] C.C. Yuan, R. Liu, C.M. Pang, et al., Anelastic and viscoplastic deformation in a Fe-based metallic glass, *J. Alloy. Compd.* 853 (2021) 157233.
- [29] J.D. Ferry, *Viscoelastic properties of polymers*, third ed., John Wiley & Sons, 1980, p. 369.
- [30] S.K. Banerjee, On a generalized approach to first and second order magnetic transitions, *Phys. Lett.* 12 (1964) 16–17.
- [31] C.M. Pang, L. Chen, H. Xu, et al., Effect of Dy, Ho, and Er substitution on the magnetocaloric properties of Gd-Co-Al-Y high entropy bulk metallic glasses, *J. Alloy. Compd.* 827 (2020) 154101.
- [32] L. Xue, L.L. Shao, Q. Luo, et al.,  $Gd_{25}Re_{25}Co_{25}Al_{25}$  (Re = Tb, Dy and Ho) high-entropy glassy alloys with distinct spin-glass behavior and good magnetocaloric effect, *J. Alloy. Compd.* 790 (2019) 633–639.
- [33] Y. Fang, J. Du, B.L. Shen, Controllable spin-glass behavior and large magnetocaloric effect in Gd-Ni-Al bulk metallic glasses, *Appl. Phys. Lett.* 101 (2012) 032405.
- [34] J. Du, Q. Zheng, Y.B. Li, et al., Large magnetocaloric effect and enhanced magnetic refrigeration in ternary Gd-based bulk metallic glasses, *J. Appl. Phys.* 103 (2008) 023918.

- [35] J.T. Zhu, Q. Luo, M.J. Cai, et al., Magnetocaloric performance and its linear relationship with magnetoresistance in Gd-Al-Cu metallic glass, *J. Magn. Magn. Mater.* 507 (2020) 166828.
- [36] L. Xia, Q. Guan, D. Ding, et al., Magneto-caloric response of the Gd<sub>60</sub>Co<sub>25</sub>Al<sub>15</sub> metallic glasses, *Appl. Phys. Lett.* 105 (2014) 192402.
- [37] Y.Q. Dong, B.G. Shen, J. Chen, et al., Large magnetic refrigerant capacity in Gd<sub>71</sub>Fe<sub>3</sub>Al<sub>26</sub> and Gd<sub>65</sub>Fe<sub>20</sub>Al<sub>15</sub> amorphous alloys, *J. Appl. Phys.* 105 (2009) 053908.
- [38] B. Schwarz, B. Podmilsak, N. Mattern, et al., Magnetocaloric effect in Gd-based Gd<sub>60</sub>Fe<sub>x</sub>Co<sub>30-x</sub>Al<sub>10</sub> metallic glasses, *J. Magn. Magn. Mater.* 322 (2010) 2298–2303.
- [39] S.A. Uporov, R.E. Ryltsev, V.A. Bykov, et al., Glass-forming ability, structure and magnetocaloric effect in Gd-Sc-Co-Ni-Al bulk metallic glasses, *J. Alloy. Compd.* 854 (2021) 157170.
- [40] L. Xia, C. Wu, S.H. Chen, et al., Magneto-caloric effect of a Gd<sub>50</sub>Co<sub>50</sub> amorphous alloy near the freezing point of water, *AIP Adv.* 5 (2015) 097122.
- [41] B.Z. Tang, L.W. Huang, M.N. Song, et al., Compositional dependence of magnetic and magnetocaloric properties of the Gd-Ni binary amorphous alloys, *J. Non Cryst. Solids* 522 (2019) 119589.
- [42] Z.G. Zheng, X.C. Zhong, H.Y. Yu, et al., The magnetocaloric effect and critical behavior in amorphous Gd<sub>60</sub>Co<sub>40-x</sub>Mn<sub>x</sub> alloys, *J. Appl. Phys.* 111 (2012) 07A922.
- [43] M.N. Song, L.W. Huang, B.Z. Tang, et al., Enhanced curie temperature and magnetic entropy change of Gd<sub>50</sub>Co<sub>50-x</sub>Ni<sub>x</sub> amorphous alloys, *Mod. Phys. Lett. B* 34 (2020) 2050050.
- [44] P. Yu, C. Wu, Y.T. Cui, et al., Excellent magneto-caloric effect of a low cost Gd<sub>34</sub>Ni<sub>22</sub>Co<sub>11</sub>Al<sub>33</sub> metallic glass, *Mater. Lett.* 173 (2016) 239–241.
- [45] G.L. Liu, D.Q. Zhao, H.Y. Bai, et al., Room temperature table-like magnetocaloric effect in amorphous Gd<sub>50</sub>Co<sub>45</sub>Fe<sub>5</sub> ribbon, *J. Phys. D* 49 (2016) 055004.
- [46] P. Yu, N.Z. Zhang, Y.T. Cui, et al., Achieving better magneto-caloric effect near room temperature in amorphous Gd<sub>50</sub>Co<sub>50</sub> alloy by minor Zn addition, *J. Non Cryst. Solids* 434 (2016) 36–40.
- [47] P. Jia, L. Duan, K. Wang, et al., Magnetic properties and magnetocaloric effects of Gd<sub>65</sub>(Cu Co, Mn)<sub>35</sub> amorphous ribbons, *J. Mater. Sci. Technol.* 35 (2019) 2283–2287.
- [48] Q.Y. Dong, B.G. Shen, J. Chen, et al., Magnetic properties and magnetocaloric effects in amorphous and crystalline GdCuAl ribbons, *Solid State Commun.* 149 (2009) 417–420.
- [49] L. Li, C. Xu, Y. Yuan, S. Zhou, Large refrigerant capacity induced by table-like magnetocaloric effect in amorphous Er<sub>0.2</sub>Gd<sub>0.2</sub>Ho<sub>0.2</sub>Co<sub>0.2</sub>Cu<sub>0.2</sub> ribbons, *Mater. Res. Lett.* 6 (2018) 413–418.
- [50] J.T. Huo, L.S. Huo, H. Men, et al., The magnetocaloric effect of Gd-Tb-Dy-Al-M (M=Fe, Co and Ni) high-entropy bulk metallic glasses, *Intermetallics* 58 (2015) 31–35.
- [51] Q. Luo, D.Q. Zhao, M.X. Pan, et al., Magnetocaloric effect in Gd-based bulk metallic glasses, *Appl. Phys. Lett.* 89 (2006) 081914.
- [52] T.D. Shen, R.B. Schwarz, J.Y. Coulter, et al., Magnetocaloric effect in bulk amorphous Pd<sub>40</sub>Ni<sub>22.5</sub>Fe<sub>17.5</sub>P<sub>20</sub> alloy, *J. Appl. Phys.* 91 (2002) 5240–5245.
- [53] S. Atalay, H. Gencer, V.S. Kolat, Magnetic entropy change in Fe<sub>74-x</sub>Cr<sub>x</sub>Cu<sub>1</sub>Nb<sub>3</sub>Si<sub>13</sub>B<sub>9</sub> (x = 14 and 17) amorphous alloys, *J. Non Cryst. Solids* 351 (2005) 2373–2377.
- [54] J.H. Belo, J.S. Amaral, A.M. Pereira, et al., On the curie temperature dependency of the magnetocaloric effect, *Appl. Phys. Lett.* 101 (2012) 079904.
- [55] L. Xue, L.L. Shao, Z.Z. Li, et al., Utilization of high entropy in rare earth-based magnetocaloric metallic glasses, *J. Mater. Res. Technol.* 18 (2022) 5301–5311.
- [56] Y. Yuan, Y. Wu, X. Tong, H. Zhang, H. Wang, X.J. Liu, et al., Rare-earth high-entropy alloys with giant magnetocaloric effect, *Acta Mater.* 125 (2017) 481–489.
- [57] Y. Yang, J. Zhou, F. Zhu, et al., Determining the three-dimensional atomic structure of an amorphous solid, *Nature* 592 (2021) 60–64.
- [58] J.M. Maita, G. Song, M. Colby, et al., Atomic arrangement and mechanical properties of chemical-vapor-deposited amorphous boron, *Mater. Design* 193 (2020) 10885.
- [59] L. Xia, K.C. Chan, Enhanced magnetocaloric effect of a partially crystalline Gd<sub>55</sub>Al<sub>20</sub>Ni<sub>25</sub> bulk metallic glass, *Solid State Sci.* 13 (2011) 2086–2089.